Universal Fabrication of Highly Efficient Plasmonic Thin-Films for Label-Free SERS Detection

Sara Gullace,† Verónica Montes-García,† Victor Martín, David Larios, Valentina Girelli Consolaro, Fernando Obelleiro, Giuseppe Calogero, Stefano Casalini, Paolo Samorì**

Dr. S. Gullace, Dr. V. Montes-García, Dr. S. Casalini, Prof. P. Samorì
University of Strasbourg, CNRS, ISIS UMR 7006, 8 Alleé Gaspard Monge, 67000 Strasbourg, France. E-mail: samori@unistra.fr

Dr. S. Gullace
Department of Chemical, Biological, Pharmaceutical and Environmental Sciences, University of Messina, V.le F. Stagno d'Alcontres 31, 98166 Messina, Italy.

Dr. S. Casalini
Università degli Studi di Padova, Dipartimento di Scienze Chimiche, via Marzolo 1, Padova 35131, Italy. E-mail: stefano.casalini@unipd.it

Dr. G. Calogero
IPCF-CNR, Istituto per i Processi Chimico-Fisici, V.le F. Stagno d'Alcontres 37, 98158 Messina, Italy.

V. Martín, D. Larios
Departamento Tecnología de los Computadores y de las Comunicaciones, Universidad de Extremadura, 10003 Cáceres, Spain.

V. Girelli Consolaro
Université de Strasbourg, CNRS, IPCMS UMR 7504
23 rue du Loess, F-67034 Strasbourg, France.

Prof. F. Obelleiro
Departamento de Teoría de la Señal y Comunicaciones, Universidade de Vigo, 36310 Vigo, Spain.

† These authors equally contributed to this work.

Keywords: plasmonic thin-films, SERS sensing, metal nanoparticles, core-shell, graphene oxide, layer-by-layer assembly

Abstract

The development of novel, highly efficient, reliable, and robust surface-enhanced Raman scattering (SERS) substrates containing a large number of hot spots with programmed size, geometry and density is extremely interesting since it allows the chemical sensing of numerous (bio-)chemical species. Herein, an extremely reliable, easy to fabricate and label-free SERS sensing platform based on metal nanoparticles (NPs) thin-film is developed by the layer-by-layer growth mediated by polyelectrolytes. A systematic study of the effect of NP composition and size as well as number of deposition steps on the substrate's performance is accomplished by monitoring the SERS enhancement of 1-naphtalenethiol, using a 532 nm excitation. Distinct evidence of the key role played by the interlayer (poly(diallyldimethylammonium chloride) (PDDA) or PDDA-functionalized graphene oxide (GO@PDDA)) on the overall SERS efficiency of the plasmonic platforms is provided, revealing in the latter the formation of more uniform hot spots by regulating the interparticle distances to 5 ± 1 nm. Our SERS platform efficiency is demonstrated via its high analytical enhancement factor (~10^6) and the detection of a prototypical substance, i.e. drug tamoxifen (TAM), both in Milli-Q water and in a real matrix, viz. tap water, opening perspectives towards the use of our plasmonic platforms for future high-performance sensing applications.

1. Introduction

Surface-enhanced Raman scattering (SERS) spectroscopy is an extremely powerful analytical technique for the highly sensitive, and non-invasive chemical identification of multiple (bio-)chemical analytes.[1] Indeed, SERS (indirect or label-free) allows identification of the specific spectral fingerprint of probe analytes in close contact with a plasmonic substrate (i.e. noble metal nanostructures).[2] Importantly, SERS offers multiplexing capability, it requires little or no sample preparation, and it provides high spatial resolution in sample mapping. Within this context, SERS detection has been applied in several fields such as medical diagnostics,[3] environmental protection,[4] and food safety.[5] Because of the low Raman cross-section of many analytes, rational design and engineering of SERS substrates are crucial in order to collect SERS signals with high sensitivity, tunability, reproducibility and stability.[6] The presence of the so-called "hot spots" (such as junctions or gaps between metal NPs on the nm scale) in sufficient density on the substrate surface can markedly enhance the sensing capabilities of any SERS platform, allowing to reach lower limits of detection which is crucial for many applications.[7] In fact, it has been reported that a hot spot can produce enhancements of SERS intensity up to 15 orders of magnitude (proportional to $|E|^4$) reaching single molecule detection.[8] Such colossal sensitivity enhancement has triggered a major research endeavour on the fabrication of plasmonic substrates containing a high density of hot spots. Nevertheless, the controlled fabrication of plasmonic substrates containing hot spots with designed size, geometry and density over an extensive area is still a challenge in terms of batch-to-batch reproducibility and large-scale homogeneity. Hot spots can be produced either via the assembly of nanoparticles in colloidal dispersion[9] or by preparing nanostructured surfaces using lithographic techniques,[10] as focused ion beam milling,[11] or by depositing nanoparticles onto solid supports.[4] Despite the several advantages of colloidal NPs in solution (i.e. high reproducibility, cost-effectiveness, or tailored optical properties),[12] it is well-known that hot spots can only be achieved through dynamic and uncontrolled aggregation processes, usually

taking place in the presence of the analyte. Aggregation heavily affects and limits the overall robustness of these SERS sensors in real life applications, since the reproducibility of the spectra is strongly dependent on the experimental conditions.[1] Although nanofabrication techniques (e.g., lithography-based like focused ion beam milling) allow for large-scale production, they also present uncompelling disadvantages, such as high cost and low resolution to reach lengthscale less than 10 nm. For all these reasons, a compelling alternative is represented by the direct self-assembly of colloidal NPs onto a solid support, towards the generation of operational devices suitable for commercialization.[13] In this framework, numerous strategies have been explored to achieve the controlled immobilization of NPs on solid supports, aiming to large surface sensing substrates with high enhancement and reproducibility.[14] Among them, the layer-by-layer (LbL) growth has emerged as one of the most powerful approaches for the fabrication of nanostructured thin-films[4] with tailored composition, structure, and thickness[15] on any surface, regardless of its shape and/or size. The growth process is ruled by either electrostatic or non-electrostatic interactions (i.e. hydrogen bonding, metal-ion coordination, host−guest interaction, covalent bonds, and so on).[16] In essence, this technology can be considered highly versatile, simple, and efficient, and as such, it holds great potential for the fabrication of SERS substrates. Although different components have been proposed as interlayer for the alternate LbL assembly with metal nanoparticles including polyelectrolytes,[17] macrocycles,[4] dendrimers[18] and nanosheets,[19] poor attention has been given to the key parameters to boost the SERS performance, such as the NP's composition, size and shape as well as control of the interparticle distance, being pivotal for the hot spot optimization. Crozier and co-workers have shown that the SERS enhancement increases when the interparticle distance in Au NP dimers decreases from 10 to 0.6 nm, while also a substantial drop is observed as the interparticle distance is reduced down to 0.2 nm, due to the strong electromagnetic (EM) field confinement.[20] Recent developments operating under strict electrodynamic conditions revealed that the EM field does not follow the predicted

behaviour of $|E|^4 \sim 1/a^4$ (where a is the interparticle distance) but it satisfies universal behaviour, yielding an expression $|E|^4 \sim 1/a^p$ (with $p \approx 1.2\text{-}1.5$).[21] This discrepancy is associated with the emergence of electron tunnelling between the particles as the interparticle distance becomes less than 2 nm.[20] Once the interparticle distances reach sub-nm (< 1 nm) size, the classical electromagnetic approach fails, and the non-local effects, such as the strong EM field confinement, come into play. [21] Hence, the ideal interparticle distance leading to the highest SERS enhancement should be comprised in the 1-10 nm range. However, while the majority of the studies on the hot spot engineering have been performed on Au NPs, the scenario is not well established yet in the case of Ag NPs and on more sophisticated metallic NPs compositions.

Herein, we report the fabrication of reliable, and label-free SERS sensing platforms, constituted by Ag and Au@Ag core@shell NPs thin-films assembled via the LbL technique, with an accurate design and engineering of the hot spot size and density. The thin-films supported on glass supports were manufactured by the alternate deposition of negatively charged (tannic acid)/citrate coated metal NPs and the positively charged poly(diallyldimethylammonium chloride) (PDDA) polyelectrolyte, held together by electrostatic interactions. We have studied the plasmonic response and the morphology (structure and hot spot density) of the films as a function of the NP composition (by exploring Ag, and Au@Ag core@shell NPs), the NP size (from 15 to 89 nm), the number of deposition steps (1 to 4) and the influence of an interlayer such as (poly(diallyldimethylammonium chloride) (PDDA) or PDDA-functionalized graphene oxide (GO@PDDA). Subsequently, the SERS performances for the different NPs platforms were investigated with a 532 nm laser line by employing 1-naphthalenethiol (1-NAT) as Raman reporter as well as other molecules such as methylene blue, methyl orange and dopamine. Finally, the sensitivity of the best SERS platform was analysed for the label free detection of the antineoplastic drug tamoxifen (TAM) in tap water.

2. LbL assembly of metal NPs

Thin-films of (tannic acid) / citrate-stabilized metal nanospheres[22] have been controllably assembled by the LbL technique via the subsequent deposition of oppositely charged building blocks, i.e. negatively charged (tannic acid) / citrate -stabilized metal nanospheres and a cationic polyelectrolyte, poly(diallyldimethylammonium chloride) (PDDA).[4]

In particular, the metal NPs assemblies have been grown onto glass supports following the mechanism portrayed in Scheme 1: first, to ensure an optimal distribution of positive charges on the surfaces, a triple layer of oppositely charged polyelectrolytes was deposited. This was obtained by immersing activated glass supports in an aqueous polycationic PDDA solution (0.1 mg/mL, NaCl 0.5 M) followed by their immersion in an aqueous polyanionic poly(acrylic acid) (PAA) solution (0.1 mg/mL, NaCl 0.5 M) and then in PDDA, once again. Subsequently, such positively charged surfaces were exposed to an aqueous dispersion of negatively charged (tannic acid) /citrate-stabilized metal NPs (scheme 1, step I). PDDA and (tannic acid) / citrate-stabilized metal NPs, hereafter PDDA – metal NPs, deposition steps were alternatively repeated to produce controlled nanoparticle assemblies (scheme 1, step II, III and IV). Four PDDA - metal NPs deposition steps were performed in total.

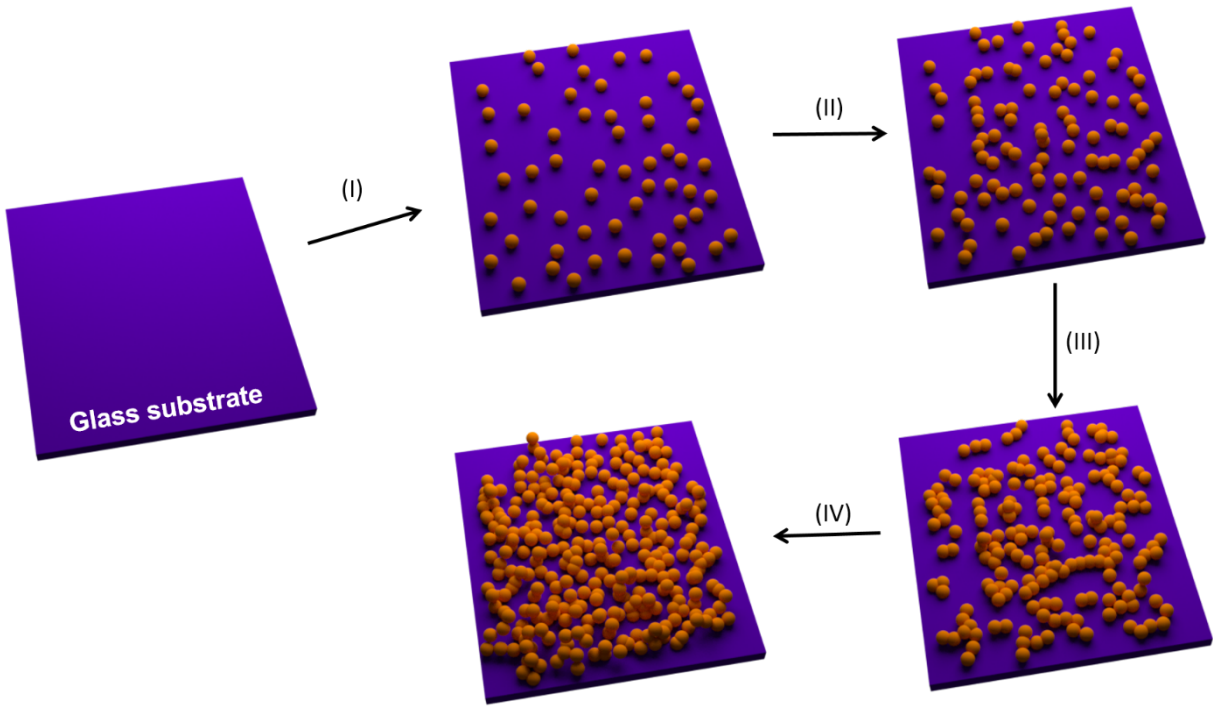

Scheme 1. Schematic representation of assemblies of metal NP fabricated by electrostatic Layer-by-Layer deposition. Step I consists of a triple layer of oppositely charged polyelectrolytes (PDDA - PAA - PDDA). Steps II, III and IV correspond to the subsequent immersion of the substrate in PDDA solution (0.1 mg/mL, NaCl 0.5 M) for 15 min and in an aqueous solution of metal NPs for 3h.

3. Optimization of SERS Substrates

3.1. Mono-component metal NPs

Despite the inherently higher SERS activity of Ag compared to Au,[23] sensing platforms based on Ag NPs are more unexplored because of their poor ambient stability resulting from their spontaneous oxidation. Visible−NIR spectroscopy and scanning electron microscopy (SEM) analyses made it possible to monitor the LbL growth of the PDDA - Ag NPs hybrid. **Figure 1**a shows the optical properties of PDDA - 37 nm Ag NPs assemblies in air obtained after one, two, three, and four PDDA - Ag NPs depositions steps on glass. In the case of one deposition step film, the optical response exhibits a main localized surface plasmon resonance (LSPR) band centered at 394 nm and a less intense and broader band at 607 nm (Figure 1a). The presence of isolated Ag NPs on the substrate surface is proved by the former band, which is blue-shifted with respect to the one typical for Ag colloids in water (407 nm, Figure S1, Supporting Information) due to the lower average refractive index of air compared to water. The band at lower energies indicates the presence of a small amount of Ag aggregates, as confirmed by SEM imaging. As displayed in Figure 1b, the film prepared via one deposition step mostly exhibits Ag NPs randomly distributed and well separated from each other of a few tens of nanometers, although a small percentage of dimers, trimers, and tetramers is also observed. When a second deposition step was accomplished, the optical response showed a broadening in the LSPR coupling band (> 730 nm), along with an increase in extinction (Figure 1a). The optical response indicates that a larger number of particles are deposited on the surface,

resulting in the formation of Ag NPs assemblies causing an intense plasmon coupling among particles, and therefore hot spots. The greater interparticle interactions upon increased deposition steps, as observed by optical spectroscopy, is confirmed by SEM imaging (Figure 1b-e). The same LbL protocol to create 37 nm Ag NP films has been successfully exploited to assemble Ag NPs with different diameters (i.e. 15, 23 and 56 nm) with the alternate deposition of PDDA and tannic acid /citrate-stabilized Ag NPs, leading to a similar variation of the optical properties with the increased number of deposition steps (Figure S4, Supporting Information).

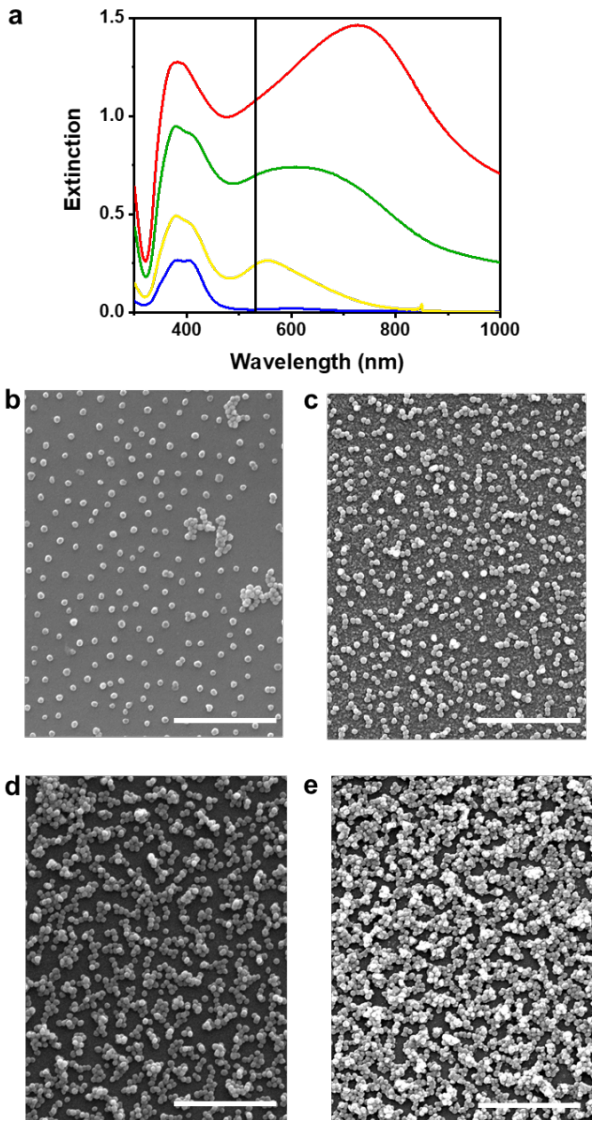

Figure 1. PDDA- 37 nm Ag NPs assemblies on activated glass: a) Visible−NIR extinction spectra recorded in air after different deposition steps: one (blue), two (yellow), three (green), and four (red). The black line highlights the position of the 532 nm laser line. b-e)

Representative SEM images obtained after b) one, c) two, d) three, and e) four deposition steps. Lateral scale bars = 1 μm.

To gain insight into the SERS performance of this new type of plasmonic substrates, we have studied the overall efficiency in terms of the number of PDDA - Ag NPs deposition steps and Ag nanoparticle size. For the SERS analysis, 1-naphthalenethiol (1-NAT) was chosen as a standard Raman reporter molecule (**Figure 2**a)[24] Prior to use, Ag NPs films were immersed for 30 min in a 50 mM $NaBH_4$ aqueous solution to remove tannic acid and citrate stabilizing agents. Figure S5 displays the SERS spectrum of the pristine 37 nm Ag NPs substrate after four deposition steps and exposure to $NaBH_4$ (black spectra) and the Raman spectra of 1-NAT (red spectra). As clearly shown, the SERS fingerprint of the plasmonic substrate does not overlap with the main characteristic peaks of 1-NAT, making it an ideal Raman reporter molecule for our SERS platform. To record the SERS spectra of 1-NAT, the plasmonic thin-films were immersed in a 10^{-5} M 1-NAT aqueous solution for 3 h and then dried under a gentle stream of N_2. Figure 2a shows a representative SERS spectrum. It revealed the characteristic signals of chemisorbed 1-NAT molecules (Table S2), including the C–H bending (1195 cm^{-1}), ring stretching (1367, 1500, and 1553 cm^{-1}), and ring breathing (818 and 964 cm^{-1}).[24-25] We focused our attention on the ring stretching of 1-NAT at 1367 cm^{-1}, which has been mapped over extended areas (typically, 40 x 40 μm^2 with 2 μm step size). Firstly, we plotted the average SERS intensity (441 points in total) at 1367 cm^{-1} (Figure 2b) as a function of deposition steps and Ag NPs size in order to evaluate the efficiency of the different plasmonic substrates. To acquire a meaningful statistic, our mappings were recorded on three different PDDA – Ag NPs plasmonic substrates, which exhibited similar intensities. Interestingly, a marked increase of the signal intensity has been observed by moving from the first to the second deposition step, independently of the Ag NPs size. This was predicted from the optical properties (Figure 1a-b and S4, Supporting Information), revealing that the one deposition substrate shows a lack of

plasmonic coupling deriving from an interparticle distance of few tens of nanometers. The third deposition step shows a further improvement of SERS signal in the case of 37 and 56 nm Ag NPs assemblies, whereas it remains nearly constant when smaller Ag NPs (viz. 15 and 23 nm) are used, presumably due to the mismatch between the excitation wavelength (532 nm) and the LSPR coupling band in the latter cases. This result is in agreement with the electromagnetic mechanism, which predicts the highest SERS intensity when the $LSPR_{max}$ is located between excitation and vibrational wavelengths, λ_{ex} and λ_{vib}, respectively.[26] Nevertheless, a plateau or a clear worsening of the signal is recorded for the fourth deposition step, independently of the NPs size. This trend is the direct effect of the stepwise increase of NPs density onto our substrate, featuring a poor control of the NPs positioning. As a result, the SERS efficiency reaches a maximum and then, an overall worsening which stems from the hot spot deactivation due to symmetry effects and differences in plasmonic coupling strength.[4, 27] A similar hot spot deactivation has been previously reported for the LbL assembly of Au nanospheres mediated by pillar[5]arene [4, 28] and for self-assembled Au nanostars on polystyrene beads,[29] where the random distribution of NPs leads to an initial increase of the SERS intensity proportional to the amount of NPs and then to an overall decrease due to the excessive and non-controllable plasmon coupling. 37 nm Ag NPs exhibited enhanced SERS efficiency compared to 56 nm ones, since, as the nanoparticles size increases, the convex shape of the surface becomes flatter, so that less inelastic scattering can occur on it, leading to a weaker electromagnetic field on the surface and a lower overall SERS intensity.[30] Finally, figure 2d-f and Figures S6-7 reveal that the intensity maps related to 1-4 deposition steps are highly uniform and homogeneous throughout the sample area, independently of the NPs size (Figure 2d-f) and number of depositions (Figures S6-7, Supporting Information). Overall, 3 deposition steps of 37 nm Ag NPs turned out being the best performing SERS platform.

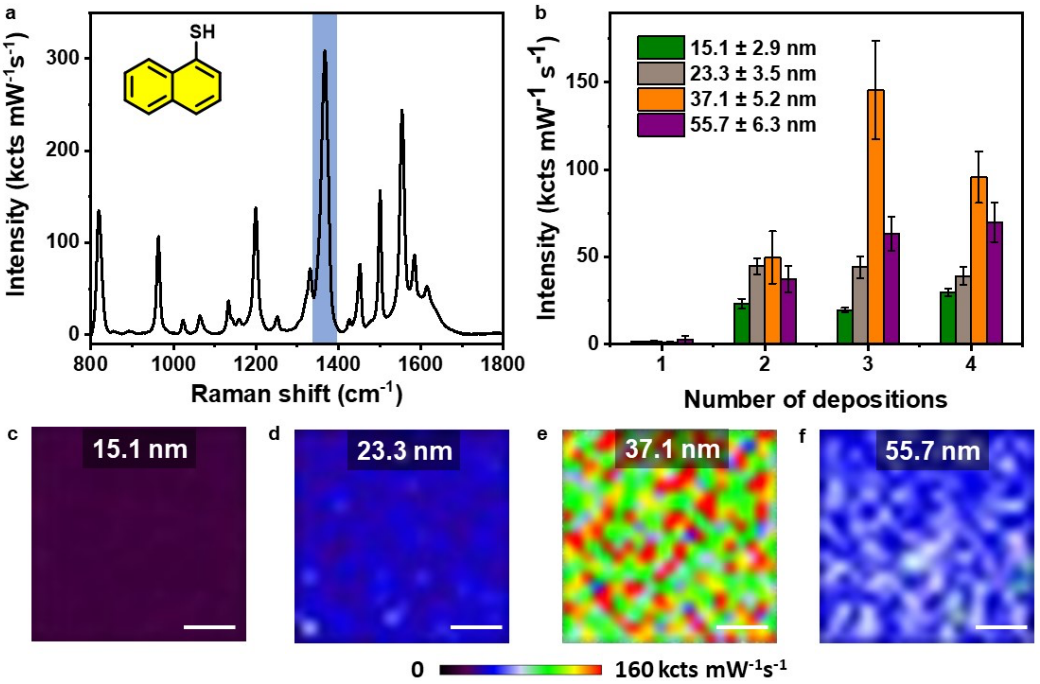

Figure 2. a) Representative SERS spectrum of 1-NAT, whose molecular structure is shown in the inset. b) Average intensities of the ring stretching band (1367 cm^{-1}) as a function of PDDA-Ag NPs deposition steps for four Ag NPs sizes. All SERS measurements were carried out with a 100× objective and a maximum power of 0.02 mW for the 532 nm laser line. The acquisition time was 1 s. c-f) SERS mappings obtained at 1367 cm^{-1} after three deposition steps of PDDA-Ag NPs as a function of Ag NPs size. Lateral scale bars = 10 μm.

3.2. Core@shell metal NPs

The metal composition of the NPs is a key parameter affecting the SERS efficiency.[31] A representative example is the one of bimetallic NPs with a core@shell structure which provides richer plasmonic modes, thanks to the combined material- and size/shape-dependent plasmonics.[32] Bimetallic core@shell NPs have been the subject of SERS studies in solution as a function of the size of both core and shell and also excitation wavelength.[22c] Samal and co-workers have shown that the SERS efficiency of the Au@Ag NPs in solution increased with size.[22c] To the best of our knowledge, a similar study on the SERS efficiency as a function of the core and shell size has never been performed in thin-film of self-assembled Au@Ag NPs.

Here we investigated the SERS effect as a function of the NPs composition using 57 nm Au@Ag NPs (Au core of 30 nm and 13 nm Ag shell) (Figure S8, Supporting Information) and 89 nm Au@Ag NPs (Au core of 50 nm and 20 nm Ag shell) (Figure 3 and S9), being the same size of the hybrid NPs reported by Samal et al,[22c] allowing us to compare results in aqueous solution with those obtained in thin solid films. Interestingly, our study of the SERS efficiency on the two different NP sizes as a function of deposition steps revealed the same behavior of the Ag NPs, i.e. the best signal was obtained at the third deposition step (Figure 3b and Figure S8b, Supporting Information) and hot spot deactivation occurs when a fourth deposition step is performed. Concerning the effect of the core@shell NPs size, we observed the same trend previously reported for colloidal systems. In particular, PDDA - 57 nm Au@Ag NPs (Au core of 30 nm and 13 nm Ag shell) assembly exhibits a LSPR maximum (780 nm) highly misaligned with the excitation wavelength, i.e. 532 nm (Figure S8), leading to a worse SERS efficiency. On the contrary, the PDDA – 89 nm Au@Ag NPs assembly displays a broad and blue-shifted extinction (LSPR maximum at 550 nm), which yields a stronger electromagnetic coupling with the excitation laser (Figure 3a and S8).

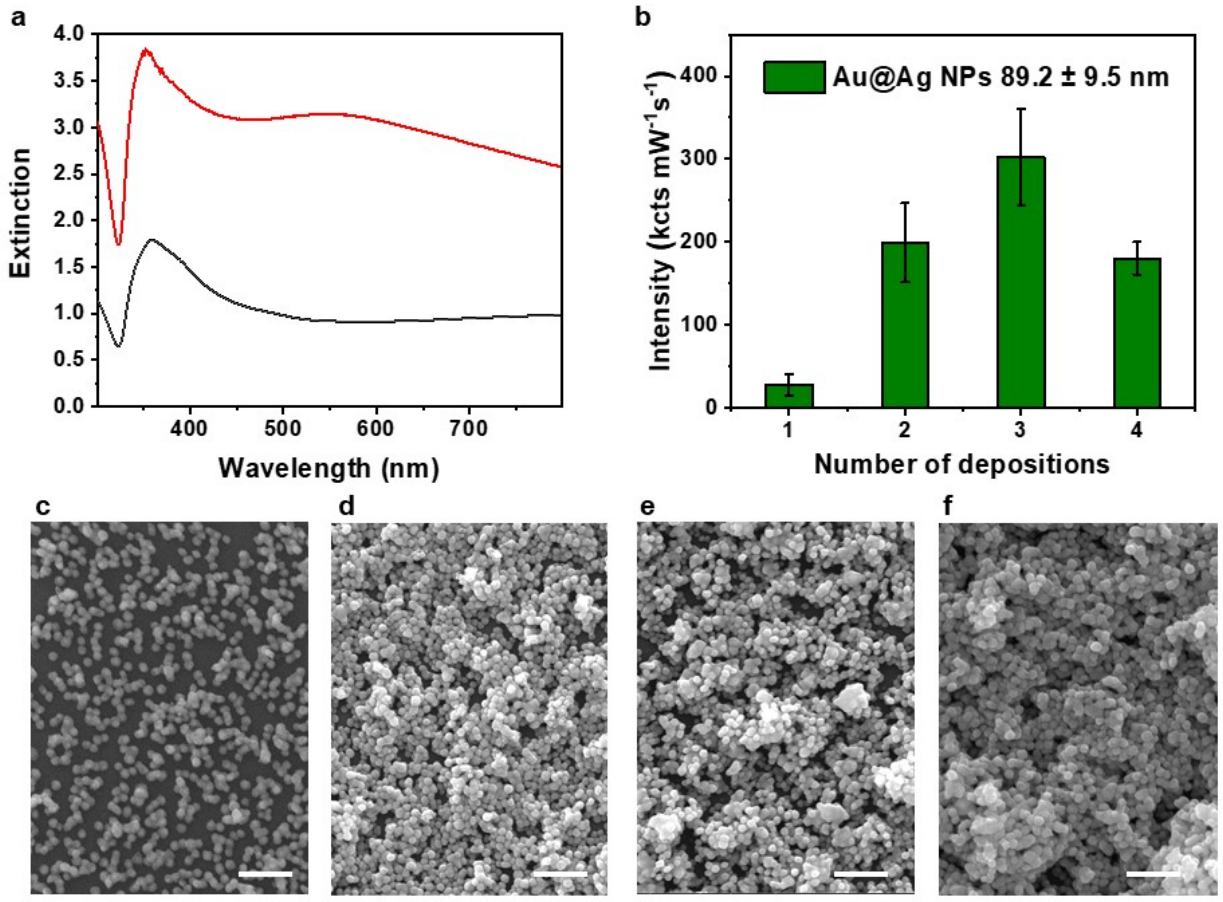

Figure 3. a) Visible−NIR extinction spectra recorded in air after different 89 nm Au@Ag NPs deposition steps: one (black spectrum), and two (red). The extinction spectra of the three and four depositions substrates were not included due to saturation. b) Average intensities of the 1-NAT ring stretching band (1367 cm^{-1}) as a function of PDDA-Au@Ag NPs depositions steps. All SERS measurements were carried out with a 100× objective and a maximum power of 0.02 mW for the 532 nm laser line. The acquisition time was 1 s. c-f) Representative SEM images of 89 nm PDDA-Au@Ag NPs assemblies on activated glass obtained after: c) one, d) two, e) three, and f) four PDDA-Au@Ag NPs deposition steps. Scale bars = 500 nm.

3.3. Interlayer effect

As aforementioned, the ideal interparticle distance leading to the highest SERS enhancement should be comprised in the range 1 - 10 nm, which can be hardly achieved when using a mono-

component PDDA film as interlayer, being the van der Waals cross-section of the macromolecule ~ 0.5 nm, when it adopts a stretched conformation. We propose a straightforward protocol to modulate the interparticle distance by varying the interlayer nature. In the present case, graphene oxide (GO) (thickness of ~ 0.8 nm) was chosen as interlayer, not only to act as a more controlled spacer but also because of its inherent SERS effect. However, the anionic nature of GO makes it unsuitable to be used as a building block for the negatively charged citrate Au@Ag NPs assembly. For this reason, GO was previously functionalized with a PDDA layer (GO@PDDA) (See experimental details in the Supporting Information), leading to an overall thickness of 5 ± 1 nm which falls in the ideal interparticle distance range. The previously used LbL protocol was employed for the fabrication of 89 nm Au@Ag NPs assemblies by using GO@PDDA as interlayer (Figure S10, Supporting Information) but exposing the plasmonic substrates to the GO@PDDA for 3 hours instead of 15 min as in the case of PDDA due to the slower kinetics of attachment of GO@PDDA (data not shown). Firstly, Figure S11 reveals that the intensity maps related to 1-4 deposition steps are highly uniform and homogeneous throughout the sample area, independently of the NPs size, number of depositions and nature of the interlayer. Interestingly, in the case of GO@PDDA, when a fourth deposition is performed, a further SERS enhancement is clearly observed for GO@PDDA – 89 nm Au@Ag NPs while not for PDDA – 89 nm Au@Ag NPs, despite these two systems show identical extinction spectra (Figure S12). The different behavior when GO is used may have two different explanations. It is well-known that GO, and more generally 2D materials, exhibit SERS effect.[33] As they support plasmons only in the terahertz region, the enhancement mechanism relies on chemical factors such as charge transfer or dipole-dipole formation. Within this context, the proper combination of metal nanoparticles and 2D materials had already led to excellent systems featuring unprecedent SERS sensitivity.[34] In addition to the contribution of GO to the overall SERS enhancement, the different trend of the SERS efficiency with the number of deposition steps can also be ascribed to GO@PDDA ensuring a better

control over the NPs positioning (more control over the interparticle distance) during the deposition steps with respect to the simple PDDA, directly influencing the plasmonic coupling. We have therefore performed two set of experiments to assess the interlayer distance in the presence of GO@PDDA: the former relies on Raman spectroscopy in order to determine the number of GO layers enveloped by PDDA, and the latter consists of using electron tomography for imaging the particles and their inter-distance. Figure S13a shows a representative Raman spectrum of GO, obtained after the immersion of a glass substrate in a diluted GO@PDDA solution overnight. A 10-fold dilution of the 0.04 mg/mL GO@PDDA solution was performed in order to isolate GO@PDDA flakes for Raman analysis. The detailed experimental procedure is reported in the Supporting Information. The Raman spectrum of GO exhibits the 2D and the overtone of the G+D peaks.[35] A distribution histogram indicates the position of the 2D peak for 5 isolated GO flakes, extrapolated from Raman mappings over the whole area of the flakes (Figure S13b). The peak position of the 2D band can be correlated with the number of GO layers: the spectral feature at 2698 and 2680 cm^{-1} can be ascribed to 3 and 5 layers in thickness, respectively. [36]

Electron tomography was performed on a hybrid system consisting of GO@PDDA functionalized with Au@Ag NPs in a colloidal solution. The detailed experimental procedure is reported in the Supporting Information. The thickness of GO@PDDA interlayer was measured from the 3D reconstruction shown in Figure S14a-e, in the area highlighted in Figure S14f. The thickness was found to range between 3 and 7 nm. These values indicate a film thickness ranging between 3.4 and 5 nm, taking into account a thickness of GO and PDDA amounting to 0.8 nm and 0.5 nm, respectively. Overall, both electron tomography and Raman spectroscopy showed that the average interparticle distance amounts to 5 ± 1 nm.

To provide strong support to our experimental evidence, plasmon-driven SERS intensities of the proposed platforms have been simulated as the product of near electric-field intensity enhancement produced upon normal irradiation with the excitation laser light and the

inelastically emitted Raman signal.[7c] This method allows the simulation of the SERS enhancement as a function of the interparticle distance, nanoparticles composition (the different metals are described through their frequency-dependent complex permittivity, taken from the optical measurements) and density on the substrate surface (Figure 4 and S15-17). [37]

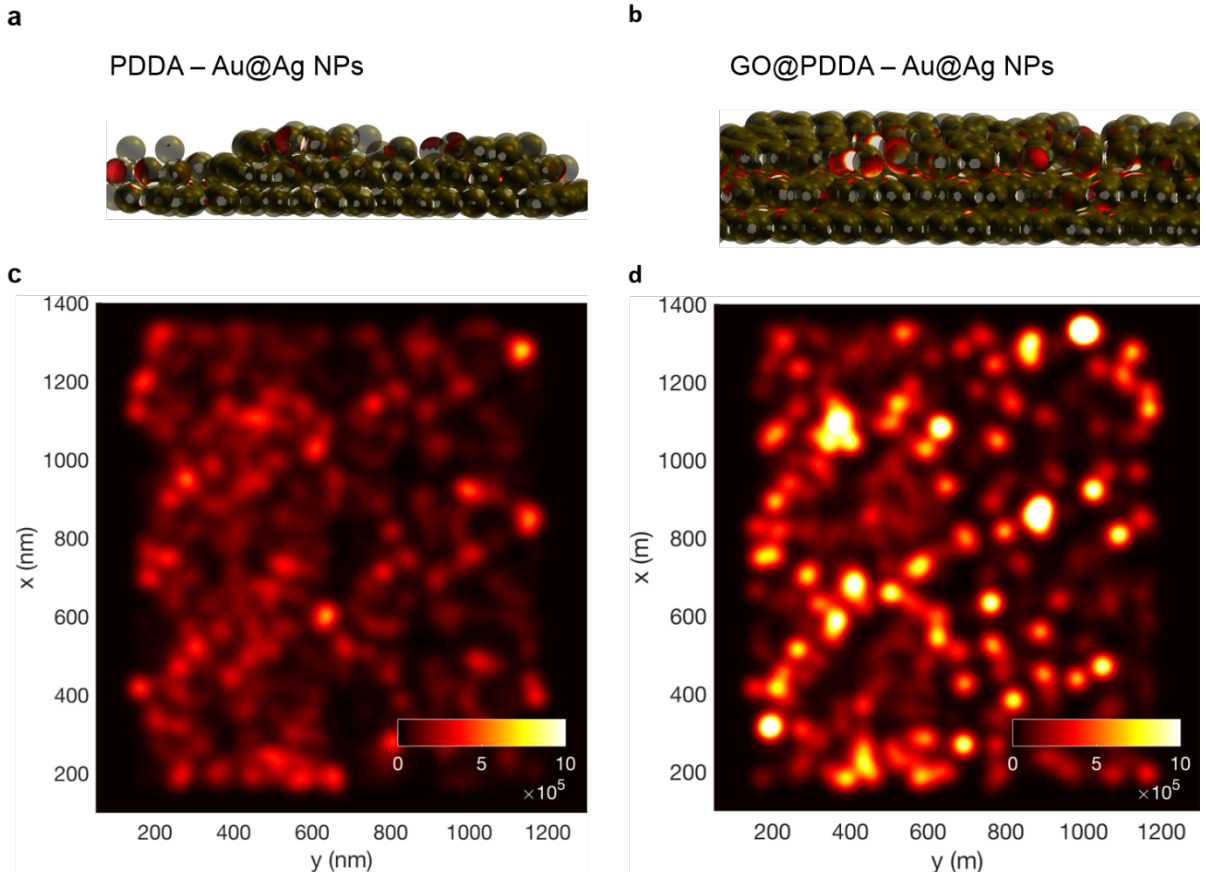

Figure 4. a-b) SERS enhancement distribution, and c-d) filtered SERS of Au@Ag NPs assemblies as a function of the adhesive layer being a,c) PDDA, and b,d) GO@PDDA.

Figure 4 clearly show the interlayer dependance NPs positioning, where controlled interparticle distances of 5 nm has led to a more efficient system, containing a higher number of hot spots which are pivotal for ultrasensitive SERS detection. The results obtained in this work varying the nature of the interlayer (PDDA vs GO@PDDA) showed that the SERS enhancement follows the same trend previously reported for NPs dimers by increasing the interparticle distance from 0.5 to 5 nm. All these findings highlight the importance of a systematic study of

the SERS performance in terms of NPs size, composition, number of deposition steps and interparticle distance to maximize the size, geometry and density of the hot spots in a reliable manner.

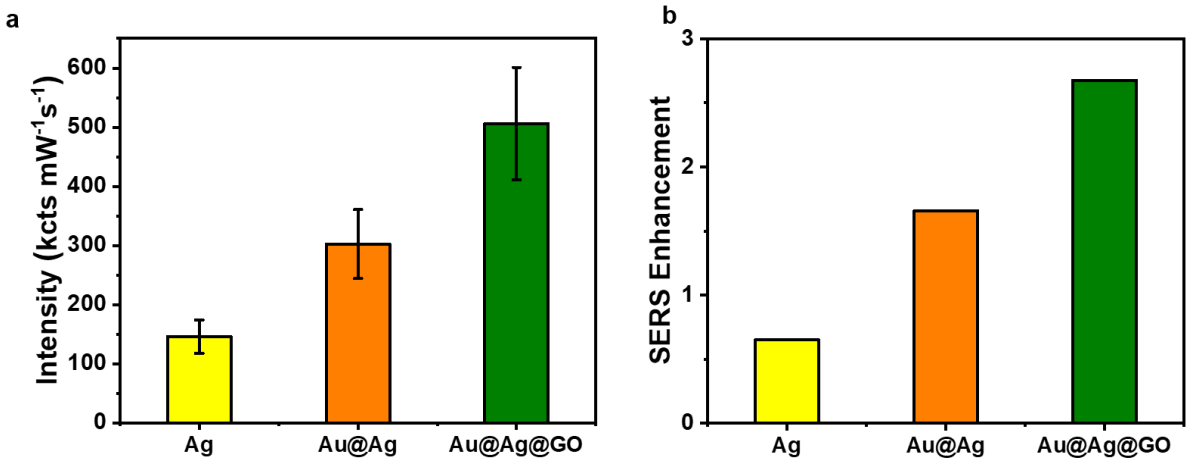

Figure 5. a) Average intensities of the 1-NAT ring stretching (1367cm^{-1}) as a function of metal NPs composition; PDDA - 37 Ag NPs (yellow), PDDA – 89 nm Au@Ag NPs (orange) and GO@PDDA – 89 nm Au@Ag NPs (green). Note that for PDDA - 37 Ag NPs and PDDA – 89 nm Au@Ag NPs the average intensity corresponds to three deposition steps, while, in the case of GO@PDDA – 89 nm Au@Ag NPs, average intensity corresponds to four deposition steps. All SERS measurements were carried out with a 100× objective and a maximum power of 0.02 mW for the 532 nm laser line. The acquisition time was 1 s. b) Simulated average SERS enhancement as a function of metal NPs composition (see the Supporting Information for details).

Figure 5a-b compares the experimental data acquired (441 points in total) at 1367 cm^{-1} with the theoretical ones stemming from the average SERS enhancement corresponding to the third deposition step for PDDA - 37 Ag NPs and PDDA – 89 nm Au@Ag NPs or fourth deposition step for the GO@PDDA – 89 nm Au@Ag NPs. Alongside, calculated SERS mappings depicting the weighted SERS for the different nanoparticle composition systems is displayed in

Figure S17. The use of GO@PDDA to modulate the assembly of 89 nm Au@Ag NPs has resulted in an enhancement in the intensity of a factor of 1.7 or 3.5 for PDDA – 89 nm Au@Ag NPs or PDDA – 37 nm Ag NPs, respectively. The SERS performance was finally quantified for GO@PDDA – 89 nm Au@Ag NPs thin-films estimating the analytical enhancement factor (AEF) which can be defined as:

$$AEF = \frac{I_{SERS}/C_{SERS}}{I_{Raman}/C_{Raman}} \quad (1)$$

with I_{SERS} being the SERS intensity at 1367 cm^{-1} of 1-NAT with a concentration C_{SERS} and I_{Raman} Raman intensity of 1-NAT with a concentration of C_{Raman} both recorded under identical experimental conditions (laser wavelength, laser power, microscope objective, spectrometer, etc.). In this particular case, the AEF obtained was ~10^6, in good agreement with AEFs reported for other metal NPs platforms.[38] Finally, 2D materials may play an additional role on the fabrication of hybrid SERS plasmonic substrates. Graphene and other 2D materials have been recently reported as a protective barrier against oxidation and corrosion processes.[34, 39] Oxidation processes, especially for Ag NPs, inevitably affect the long-term stability of SERS substrates, which is a commonly neglected but critical problem for practical applications. We have evaluated the stability of 89 nm -Au@Ag NPs assemblies when combined with both type of interlayers, i.e. PDDA or GO@PDDA (Figure S18) for 60 days. As can be seen in Figure S12, the NPs oxidation is drastically reduced for the substrates fabricated when using GO@PDDA, as the optical properties remain practically constant. On the contrary, in the case of PDDA the extinction is drastically reduced, as a consequence of the oxidation of Au@Ag NPs. Hence, the combination of plasmonic substrates with 2D materials not only boosted its SERS performance but also reinforced its long-term stability, being both characteristics of high interest for real life practical applications.

4. Sensing capabilities

Our stepwise approach to the fabrication of an efficient label-free SERS platform allows the identification of several analytes through their own Raman spectrum. Such label-free sensors can find also application in the identification and differentiation of analytes in complex matrices (i.e. tap water or biological fluids), using complex statistical models for unknown compositions.[1] In this work, we show the sensing capabilities of our best performing label-free SERS platform (*viz.* GO@PDDA- 89 nm Au@Ag NPs) for the detection of different molecules. In particular, in Figure S14 we display the comparison between the SERS and Raman spectra of methylene blue, methyl orange and dopamine. The most significant and typical bands for these target molecules are clearly visible and enhanced in the SERS spectra, while most of them are not clearly discernible in the Raman spectra. Furthermore, the N-Ag stretching band is also visible at ~237 cm^{-1}, suggesting that the adsorption of those molecules occurs via N.[40] The Tables S3-5 report a detailed vibrational band assignment for methylene blue, methyl orange and dopamine. Furthermore, we challenge our label-free SERS platform practical applicability to track tamoxifen (TAM), a well-known anticancer drug that can be used against estrogen receptor-positive breast cancer cells.[41] It has been demonstrated that many cytotoxic drugs are present in hospital effluents as well as in aquifer.[42] Furthermore, TAM can lead to corneal toxicity [43] and hence its accurate and fast detection is of high importance in terms of diagnosis.

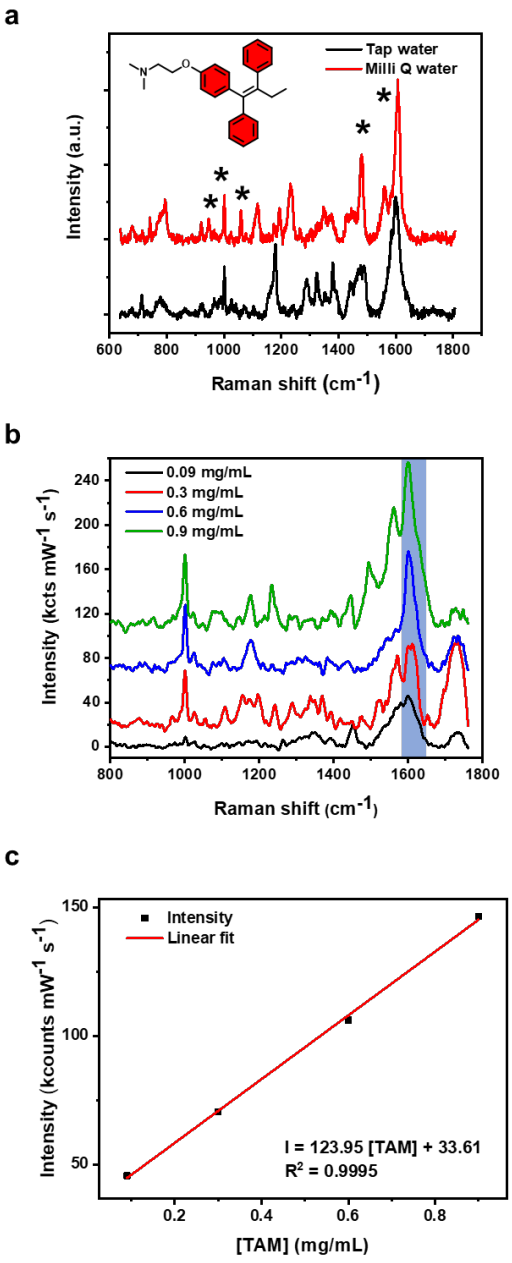

Figure 6. a) Representative SERS spectrum of 0.9 mg/mL tamoxifen in Milli Q and tap water. The acquisition time was 10 s. The main peaks are highlighted with a star. b) SERS TAM spectra at different concentrations. All the spectra were acquired after drop casting of 5 µL of the TAM solution in Milli Q water. All the SERS measurements were carried out with a 100× objective and a maximum power of 0.02 mW for the 532 nm laser line. The acquisition time was 1 s and 20 accumulations were collected. c) SERS intensity at 1611 cm^{-1} as a function of tamoxifen concentration.

Thus, as a proof-of-concept, we investigated its detection both in Milli Q and tap water by drop casting 20 µl of TAM aqueous samples (0.9 mg/mL) on our best performing SERS platform (viz. GO@PDDA- 89 nm Au@Ag NPs). The SERS recording has been performed after air-drying (**Figure 6a**). Table S6 shows a detailed vibrational band assignment for TAM. Figure 6a displays a representative vibrational spectrum acquired for TAM in Milli Q (red spectrum) and tap water (black spectrum). Interestingly, the characteristic TAM peaks were clearly distinguished and compared in the two samples. It was found that the SERS intensities were similar, suggesting no matrix interferences. In other words, our platform can be used as disposable and single shot selective sensor. In fact, our device is capable to detect the spectroscopic TAM fingerprints in a real matrix like tap water with a sensitivity in the ppm range, thus complying with the state of the art of plasmonic sensors and ultimately matching the nowadays commercial requirements. To demonstrate the sensing capabilities of such plasmonic substrate, we investigated the limit of detection (LoD) and the sensitivity towards TAM. It was performed by drop-casting (TAM volume droplet corresponding to 5 µL) on the plasmonic substrate at different concentrations (0.09 – 0.9 mg/mL) and recording their SERS spectra. A linear variation of the SERS signal is observed as a function of the analyte concentration (Figure 6b-c). The SERS measurements showed the feasibility to achieve a quantitative TAM detection within the above-mentioned range of concentrations. The final sensitivity corresponds to 123.95 mL/mg and a linear response has been defined by the following formula: I = 123.95 [TAM] + 33.61 (R^2 = 0.9995), where I is the SERS intensity (in kcounts/mW s) and [TAM] is the TAM concentration (in mg/mL). The LoD of such sensing platform has been calculated as 3.3×10^{-2} mg/mL as:

$$LoD = \frac{(3\ SD)}{\sigma} \quad (2)$$

where SD is the standard error of the regression and σ is the sensitivity. To the best of our knowledge, there is only one published paper showing the SERS detection of TAM, where the

lowest detected concentration is 3.7×10^{-1} mg/mL.[38] The detection of cytostatic drugs such as TAM in water or sewage effluent and surface waters is usually based on chromatographic methods associated to mass spectrometry, as shown in Table S1. Despite the extremely low LoD up to ~10^{-10} mg/mL in the case of TAM,[44] these sophisticated methods are standard bench analysis, which cannot be exploited for in-field analysis. Furthermore, these techniques show low response time, they are based on expensive equipments, and they require specialized personnel. Conversely, SERS spectroscopy can be adapted for the unequivocal, rapid and on-site analyte detection

5. Conclusion

In summary, we have proposed a straightforward fabrication protocol for reliable and label-free SERS platforms based on the electrostatic LbL assembly of metal nanoparticles and polyelectrolytes, with an accurate design and engineering of the hot spot size and density. The plasmonic performance was optimized based on the composition of metal NPs (single vs core@shell NPs), size of NPs (15-89 nm), number of deposition steps (1-4) and interlayer (PDDA vs GO@PDDA). The analysis of the SERS performance of the different platforms revealed that core@shell nanostructures (89 nm Au@Ag NPs), which have not been studied before as thin-films, exhibited a better performance compared to mono-component metal NPs (vs 37 nm Ag NPs) due to their inherent unique plasmonic modes. In addition, the use of GO@PDDA as building block ensured the formation of more uniform hot spots by regulating the interparticle distances to 5 ± 1 nm, leading to an increase in the overall SERS efficiency and a robust shelf-life (viz. at least 60 days). Importantly, all the experimental findings are in accordance with the simulated SERS enhancement. Interestingly, the AEF obtained for GO@PDDA- 89 nm Au@Ag NPs thin-films was ~10^6, in good accordance with AEF reported for other metal NPs platforms. The high performance of this plasmonic platform, as a label-free SERS substrate, has been successfully tested by comparing the SERS and Raman spectra of

methylene blue, methyl orange and dopamine in Milli-Q water. A linear variation of the TAM signal is observed as a function of its concentration in the range 0.09 – 0.9 mg/mL and its LoD was calculated as 3×10^{-2} mg/mL in Milli Q water. Furthermore, our SERS platform succeeded to detect TAM even in tap water, as a result of the excellent capability of this sensor. Finally, such results meet the stringent requirements of in-field sensing applications, making this technology a promising route to be explored towards the development of novel SERS sensors.

Supporting Information

Supporting Information is available from the Wiley Online Library or from the author.

Acknowledgements

The authors acknowledge funding from European Commission through the AMI project funded by the ERA-NET EuroNanoMed III programme, the European Union and the Agence Nationale de la Recherche (ANR) GA-ANR-17-ENM3-0001-01, the Marie Sklodowska-Curie projects ITN project BORGES (GA-813863), ERC project SUPRA2DMAT (GA-833707), the Graphene Flagship Core 3 project (GA- 881603), the Agence Nationale de la Recherche through the Labex projects CSC (ANR-10-LABX-0026 CSC), and NIE (ANR-11-LABX-0058 NIE) within the Investissement d'Avenir program (ANR-10-120 IDEX-0002- 02), the International Center for Frontier Research in Chemistry (icFRC) and the Institut Universitaire de France (IUF). S.G. acknowledges the Research & Mobility 2017 Project ARCADIA - smARt materials for landfill leaChAte remeDIAtion. This work was supported in part by the European Regional Development Fund (ERDF) and the Spanish Ministerio de Ciencia, Innovación y Universidades under Project TEC2017-85376-C2-1-R and Project TEC2017-85376-C2-2-R and in part by the ERDF and the Galician Regional Government as part of the agreement for funding the Atlantic Research Center for Information and Communication Technologies (AtlantTIC).

Received: ((will be filled in by the editorial staff))
Revised: ((will be filled in by the editorial staff))
Published online: ((will be filled in by the editorial staff))

References

[1] J. Langer, D. Jimenez de Aberasturi, J. Aizpurua, R. A. Alvarez-Puebla, B. Auguié, J. J. Baumberg, G. C. Bazan, S. E. J. Bell, A. Boisen, A. G. Brolo, J. Choo, D. Cialla-May, V. Deckert, L. Fabris, K. Faulds, F. J. García de Abajo, R. Goodacre, D. Graham, A. J. Haes, C. L. Haynes, C. Huck, T. Itoh, M. Käll, J. Kneipp, N. A. Kotov, H. Kuang, E. C. Le Ru, H. K. Lee, J.-F. Li, X. Y. Ling, S. A. Maier, T. Mayerhöfer, M. Moskovits, K. Murakoshi, J.-M. Nam, S. Nie, Y. Ozaki, I. Pastoriza-Santos, J. Perez-Juste, J. Popp, A. Pucci, S. Reich, B. Ren, G. C. Schatz, T. Shegai, S. Schlücker, L.-L. Tay, K. G. Thomas, Z.-Q. Tian, R. P. Van Duyne, T. Vo-Dinh, Y.

Wang, K. A. Willets, C. Xu, H. Xu, Y. Xu, Y. S. Yamamoto, B. Zhao, L. M. Liz-Marzán, *ACS Nano* **2020**, 14, 28.
[2] S. Schlücker, *Angew. Chem. Int. Ed.* **2014**, 53, 4756.
[3] S. McAughtrie, K. Faulds, D. Graham, *J. Photochem. Photobiol. C* **2014**, 21, 40.
[4] V. Montes-García, B. Gómez-González, D. Martínez-Solís, J. M. Taboada, N. Jiménez-Otero, J. de Uña-Álvarez, F. Obelleiro, L. García-Río, J. Pérez-Juste, I. Pastoriza-Santos, *ACS Appl. Mater. Interfaces* **2017**, 9, 26372.
[5] T. Yaseen, H. Pu, D.-W. Sun, *Trends Food Sci Technol.* **2018**, 72, 162.
[6] E. C. Le Ru, E. Blackie, M. Meyer, P. G. Etchegoin, *J. Phys. Chem. C.* **2007**, 111, 13794.
[7] a) Y. Yuan, N. Panwar, S. H. K. Yap, Q. Wu, S. Zeng, J. Xu, S. C. Tjin, J. Song, J. Qu, K.-T. Yong, *Coord. Chem. Rev.* **2017**, 337, 1; b) H. Wei, H. Xu, *Nanoscale* **2013**, 5, 10794; c) D. M. Solís, J. M. Taboada, F. Obelleiro, L. M. Liz-Marzán, F. J. García de Abajo, *ACS Photonics* **2017**, 4, 329.
[8] K. Kneipp, Y. Wang, H. Kneipp, L. T. Perelman, I. Itzkan, R. R. Dasari, M. S. Feld, *Phys. Rev. Lett.* **1997**, 78, 1667.
[9] R. W. Taylor, T.-C. Lee, O. A. Scherman, R. Esteban, J. Aizpurua, F. M. Huang, J. J. Baumberg, S. Mahajan, *ACS Nano* **2011**, 5, 3878.
[10] A. D. McFarland, M. A. Young, J. A. Dieringer, R. P. Van Duyne, *J. Phys. Chem. B* **2005**, 109, 11279.
[11] Z. Li, H. T. Hattori, P. Parkinson, J. Tian, L. Fu, H. H. Tan, C. Jagadish, *J. Phys. D Appl. Phys.* **2012**, 45, 305102.
[12] V. Montes-García, M. A. Squillaci, M. Diez-Castellnou, Q. K. Ong, F. Stellacci, P. Samorì, *Chem. Soc. Rev.* **2021**, 50, 1269.
[13] a) A. R. Ferhan, D.-H. Kim, *Nano Today* **2016**, 11, 415; b) A. Shiohara, Y. Wang, L. M. Liz-Marzán, *J. Photochem. Photobiol. C* **2014**, 21, 2.
[14] R. Pilot, R. Signorini, C. Durante, L. Orian, M. Bhamidipati, L. Fabris, *Biosensors* **2019**, 9, 57.
[15] Y. Huang, X. Duan, Q. Wei, C. M. Lieber, *Science* **2001**, 291, 630.
[16] J. Borges, J. F. Mano, *Chem Rev* **2014**, 114, 8883.
[17] Z. Liu, Z. Yan, L. Bai, *Appl. Surf. Sci.* **2016**, 360, 437.
[18] R. F. Aroca, P. J. G. Goulet, D. S. dos Santos, R. A. Alvarez-Puebla, O. N. Oliveira, *Anal. Chem.* **2005**, 77, 378.
[19] R. Tian, M. Li, H. Teng, H. Luo, D. Yan, M. Wei, *J. Mater. Chem. C* **2015**, 3, 5167.
[20] W. Zhu, K. B. Crozier, *Nat. Commun.* **2014**, 5, 5228.
[21] V. Shvalya, G. Filipič, J. Zavašnik, I. Abdulhalim, U. Cvelbar, *Appl. Phys. Rev.* **2020**, 7, 031307.
[22] a) N. G. Bastús, F. Merkoçi, J. Piella, V. Puntes, *Chem. Mat.* **2014**, 26, 2836; b) N. G. Bastús, J. Comenge, V. Puntes, *Langmuir* **2011**, 27, 11098; c) A. K. Samal, L. Polavarapu, S. Rodal-Cedeira, L. M. Liz-Marzán, J. Pérez-Juste, I. Pastoriza-Santos, *Langmuir* **2013**, 29, 15076.
[23] M. Valenti, A. Venugopal, D. Tordera, M. P. Jonsson, G. Biskos, A. Schmidt-Ott, W. A. Smith, *ACS Photonics* **2017**, 4, 1146.
[24] R. A. Alvarez-Puebla, D. S. Dos Santos Jr, R. F. Aroca, *Analyst* **2004**, 129, 1251.
[25] G. Zheng, L. Polavarapu, L. M. Liz-Marzán, I. Pastoriza-Santos, J. Pérez-Juste, *Chem. Comm.* **2015**, 51, 4572.
[26] X. Zhang, C. R. Yonzon, M. A. Young, D. A. Stuart, R. P. Van Duyne, *IEE proceedings. Nanobiotechnology* **2005**, 152, 195.
[27] B. Sharma, M. Fernanda Cardinal, S. L. Kleinman, N. G. Greeneltch, R. R. Frontiera, M. G. Blaber, G. C. Schatz, R. P. Van Duyne, *MRS Bulletin* **2013**, 38, 615.

[28] T. Ogoshi, S. Kanai, S. Fujinami, T.-a. Yamagishi, Y. Nakamoto, *J. Am. Chem. Soc.* **2008**, 130, 5022.
[29] A. B. Serrano-Montes, J. Langer, M. Henriksen-Lacey, D. Jimenez de Aberasturi, D. M. Solís, J. M. Taboada, F. Obelleiro, K. Sentosun, S. Bals, A. Bekdemir, F. Stellacci, L. M. Liz-Marzán, *J. Phys. Chem. C* **2016**, 120, 20860.
[30] S. Hong, X. Li, *Journal of Nanomaterials* **2013**, 2013, 790323.
[31] J. Ma, X. Liu, R. Wang, J. Zhang, P. Jiang, Y. Wang, G. Tu, *ACS Appl. Nano Mater.* **2020**, 3, 10885.
[32] P. Guo, D. Sikdar, X. Huang, K. J. Si, W. Xiong, S. Gong, L. W. Yap, M. Premaratne, W. Cheng, *Nanoscale* **2015**, 7, 2862.
[33] J. Zhou, T. Yang, J. Chen, C. Wang, H. Zhang, Y. Shao, *Coord. Chem. Rev.* **2020**, 410, 213218.
[34] Z. Cao, P. He, T. Huang, S. Yang, S. Han, X. Wang, G. Ding, *Chem. Mat.* **2020**, 32, 3813.
[35] G. Eda, G. Fanchini, M. Chhowalla, *Nat. Nanotechnol.* **2008**, 3, 270.
[36] R. Furlan de Oliveira, P. A. Livio, V. Montes-García, S. Ippolito, M. Eredia, P. Fanjul-Bolado, M. B. González García, S. Casalini, P. Samorì, *Adv. Funct. Mater.* **2019**, 29, 1905375.
[37] P. B. Johnson, R. W. Christy, *Phys. Rev. B* **1972**, 6, 4370.
[38] M. Sakir, E. Yilmaz, M. S. Onses, *Microchem. J.* **2020**, 154, 104628.
[39] a) A. Aliprandi, T. Moreira, C. Anichini, M.-A. Stoeckel, M. Eredia, U. Sassi, M. Bruna, C. Pinheiro, C. A. T. Laia, S. Bonacchi, P. Samorì, *Adv. Mat.* **2017**, 29, 1703225; b) X. Ling, W. Fang, Y.-H. Lee, P. T. Araujo, X. Zhang, J. F. Rodriguez-Nieva, Y. Lin, J. Zhang, J. Kong, M. S. Dresselhaus, *Nano Lett.* **2014**, 14, 3033.
[40] M. Z. Si, Y. P. Kang, Z. G. Zhang, *Appl. Surf. Sci.* **2009**, 255, 6007.
[41] R. A. R. Teixeira, A. A. B. Lataliza, N. R. B. Raposo, L. A. S. Costa, A. C. Sant'Ana, *Colloids Surf. B: Biointerfaces* **2018**, 170, 712.
[42] M. Jureczko, J. Kalka, *Eur. J. Pharmacol.* **2020**, 866, 172816.
[43] L. A. Kim, D. Amarnani, G. Gnanaguru, W. A. Tseng, D. G. Vavvas, P. A. D'Amore, *IOVS* **2014**, 55, 4747.
[44] N. Negreira, M. López de Alda, D. Barceló, *J. Chromatogr. A* **2013**, 1280, 64.